Extreme thermodynamics with polymer gel tori: harnessing thermodynamic instabilities to induce large-scale deformations

Ya-Wen Chang,[1,2,*] Michael S. Dimitriyev,[1,*] Anton Souslov,[1,3,4] Svetoslav V. Nikolov,[5] Samantha M. Marquez,[6] Alexander Alexeev,[5] Paul M. Goldbart,[1] and Alberto Fernández-Nieves[1]

[1] *School of Physics, Georgia Institute of Technology, Atlanta, Georgia 30332, USA*
[2] *Present address: Department of Chemical Engineering, Texas Tech University, Lubbock, TX 79409, USA*
[3] *Leiden Institute of Physics, Leiden University, Niels Bohrweg 2, 2333 CA Leiden, Netherlands*
[4] *The James Franck Institute, University of Chicago, 929 E 57th Street, Chicago, IL 60637, USA*
[5] *George W. Woodruff School of Mechanical Engineering, Georgia Institute of Technology, Atlanta, Georgia 30332, USA*
[6] *Branford College, Yale University, New Haven, Connecticut 06520, USA*

(Dated: May 18, 2018)

When a swollen, thermoresponsive polymer gel is heated in a solvent bath, it expels solvent and deswells. When this heating is slow, deswelling proceeds homogeneously, as observed in a toroid-shaped gel that changes volume whilst maintaining its toroidal shape. By contrast, if the gel is heated quickly, an impermeable layer of collapsed polymer forms and traps solvent within the gel, arresting the volume change. The ensuing evolution of the gel then happens at fixed volume, leading to phase-separation and the development of inhomogeneous stress that deforms the toroidal shape. We observe that this stress can cause the torus to buckle out of the plane, via a mechanism analogous to the bending of bimetallic strips upon heating. Our results demonstrate that thermodynamic instabilities, i.e. phase transitions, can be used to actuate mechanical deformation in an *extreme thermodynamics* of materials.

The term "extreme mechanics" is often used in reference to mechanical structures with prescribed instabilities that enable large deformations and configurations that are hard to achieve by other means [1]. An example of this is Euler buckling, which refers to the case of a straight, slender, homogeneous elastic rod that is compressed at its ends by an applied stress [Fig. 1(a)] [2]. Below a critical stress, τ_c, there is a stable energy minimum corresponding to the deflectionless equilibrium configuration of a straight rod [Fig. 1(b), dashed curve]. In contrast, above τ_c, the energy minimum becomes a maximum and the straight rod configuration becomes unstable, with two new minima describing the stable, bent configuration of the rod [Fig. 1(b), solid curve]; this deformed state is thus achieved via a mechanical instability above τ_c.

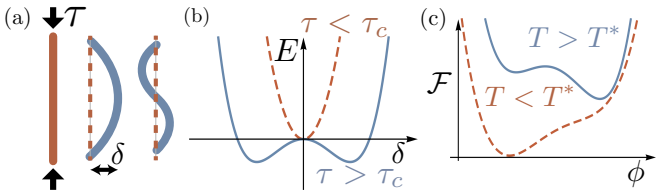

FIG. 1. (a) Elastic rod that is compressed at its ends by a tension τ. Left: straight rod; right: two examples of buckled rods. (b) Total energy of a compressed rod as a function of deflection for values of tension τ less than (dashed) and greater than (solid) a critical tension τ_c. (c) Free-energy density of a polymer gel as a function of polymer volume fraction ϕ for temperatures below a transition temperature T^*, where the gel is in the swollen phase at low ϕ, and above T^*, where it can be forced into a phase coexistent state.

Experimentally, shape actuation is often realized with polymeric materials, such as polymer gels, which are crosslinked polymer networks immersed in a solvent [3]. These respond to external stimuli by swelling or deswelling and equilibrate when the total free-energy, consisting of a polymer-solvent mixing contribution and the entropic elasticity of the polymer network, is minimized [4]. In a so-called *thermoresponsive gel*, the interplay between these two contributions to the free energy can be adjusted via temperature. Interestingly, if there are inhomogeneities in the polymer distribution within the gel, striking swelling patterns [5] can be achieved; these are oftentimes similar to the topographical features observed in soft tissues [6–8]. This strategy has also proven useful in the design of tunable surface patterns [9] and self-folding origami [10]. Importantly, in all these instances, the gel swells *quasistatically* and is thus equilibrated with the surrounding solvent bath throughout the process.

However, polymer gels can also exhibit discontinuous phase transitions between polymer-solvent mixed and segregated phases, corresponding to swollen and deswollen states. Furthermore, they can also exhibit phase coexistence where different parts of the gel are either solvent-rich or solvent-poor [3, 11]. In thermoresponsive gels below a threshold temperature, T^*, the system is in an equilibrium swollen state, where the free energy is minimum [Fig. 1(c), dashed curve]. In contrast, above T^*, the gel can exhibit phase coexistence and be characterized by a free energy with two minima [Fig. 1(c),

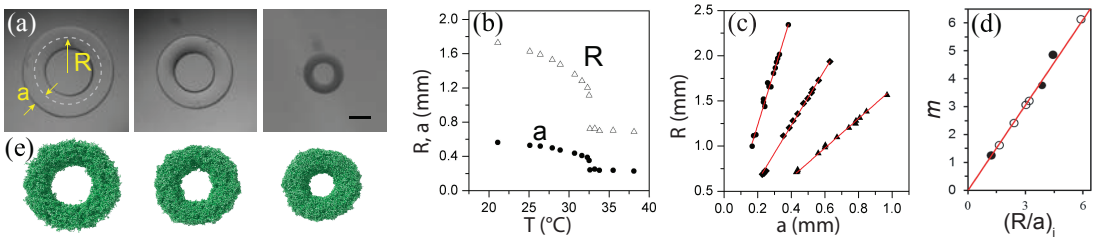

FIG. 2. (a) Quasistatic deswelling of a toroidal gel equilibrated at 25.1, 30.7, 33.5 °C. Scale bar: 1mm. (b) Temperature-dependence of the ring radius, R, and the tube radius, a, for a torus of initial aspect ratio $(R/a)_i = 3.0$. (c) R vs a for tori with an $(R/a)_i$ of (▲) 1.6, (♦) 3.0, and (●) 5.9 undergoing quasistatic deswelling. The solid lines are linear fits to the data. The intercepts of the fits are, from top to bottom (in mm): (0.02 ± 0.06) mm, (-0.037 ± 0.015) mm, and (0.042 ± 0.011) mm; these are all close to zero, consistent with deswelling happening at constant ξ. The slopes m of these fits are shown in (d) as a function of $(R/a)_i$. The closed symbols are the results obtained in computer simulations. The solid line corresponds to $m = (R/a)_i$. (e) Simulation snapshots of a toroidal gel that is deswelling quasistatically.

solid curve]. Importantly, due to the gel's shear rigidity, this last equilibrium arrangement of coexistent phases must additionally minimize the free-energy cost associated with the inhomogeneous distribution of the polymer network. Swelling equilibria thus depend on and influence the shape of the gel; the order parameter associated to the phase transition then couples to the shape, potentially affecting it in what we could call an *extreme thermodynamics* of materials. Unlike the mechanical case of Euler buckling, in this case, a thermodynamic instability is exploited to achieve large-scale material deformations.

In this Letter, we explore this idea using thermoresponsive gels made of poly-N-isopropylacrilamide (pNIPAM) and shaped as a toroid. First, we demonstrate the actuation of volume changes at fixed toroid shape. Next, we discuss our observations that after rapid heating, the toroid undergoes large shape changes and buckles out of the plane. We find that the toroid undergoes internal phase-separation at constant volume, leading to a *polarized* arrangement of solvent and polymer within its cross-section that results in a substantial internal stress difference. Through simulation and analytical modeling, we demonstrate that the observed arrangement is responsible for the toroid's buckling, confirming the notion of *extreme thermodynamics* as a means to achieve shape actuation.

We fabricate toroidal gels by first forming toroidal droplets of a precursor NIPAM solution, which is then UV-polymerized [12–14]. When heated past the lower critical solution temperature (LCST), pNIPAM gels enter a deswollen, polymer-rich phase, characterized by a small volume. Snapshots of the quasistatic evolution of a toroidal gel are shown in Fig. 2(a). Both the ring radius, R, and the tube radius, a, decrease with increasing temperature, as shown in Fig. 2(b). The rate of decrease is highest at 32.5°C, which corresponds to the LCST of pNIPAM [15]. Above this temperature, both R and a remain essentially constant, as also shown in Fig. 2(b); at these temperatures the gel is deswollen and optically opaque, as seen in the rightmost image in Fig. 2(a).

Since the gel remains isotropic and homogeneous during the quasistatic heating process, any change in the polymer matrix brought about by changes in ϕ must occur uniformly throughout the gel. Thus, all macroscopic lengths are expected to rescale by the same amount, implying that the aspect ratio of the torus, $\xi \equiv R/a$, remains unchanged. To test this, we plot R as a function of a for all tori as they deswell, and find that they are linearly related, as shown for three representative examples in Fig. 2(c). We also find there is a one-to-one correspondence between the slopes, m, obtained from the linear fits of the data, and the aspect ratio of the tori measured before deswelling. This is shown in Fig. 2(d), and confirms our expectations. We also perform dissipative particle dynamics (DPD) computer simulations to further test our results [12]. Representative snapshots of a simulated gel as it deswells are shown in Fig. 2(e). Consistent with the experimental results, R is linearly related to a, with a slope that corresponds to the aspect ratio before deswelling; the associated data points are shown in Fig. 2(d) with closed symbols.

In striking contrast with these observations, when we rapidly raise the temperature from the swollen phase at ~ 10°C to the deswollen phase at 40.0°C, the gel buckles, adopting a "Pringle$^{\text{TM}}$"-like shape, as shown for a torus with $\xi = 3.3$ in Fig. 3(a,b). This state persists over time scales from minutes to hours, depending on the overall dimensions of the torus, and eventually evolves while developing other characteristic features, as shown in Figs. 3(c,d). In spherical and cylindrical pNIPAM gels subjected to abrupt temperature changes, there is a "plateau period" over which the gel retains its original volume, followed by the formation of surface patterns [16] that are reminiscent of those we observe for tori at long-times [Figs. 3(c,d)]. The origin of this non-quasistatic evolution is the formation of a deswollen, collapsed-polymer layer, leading to extremely slow deswelling of the bulk of the gel, which, as a result, essentially main-

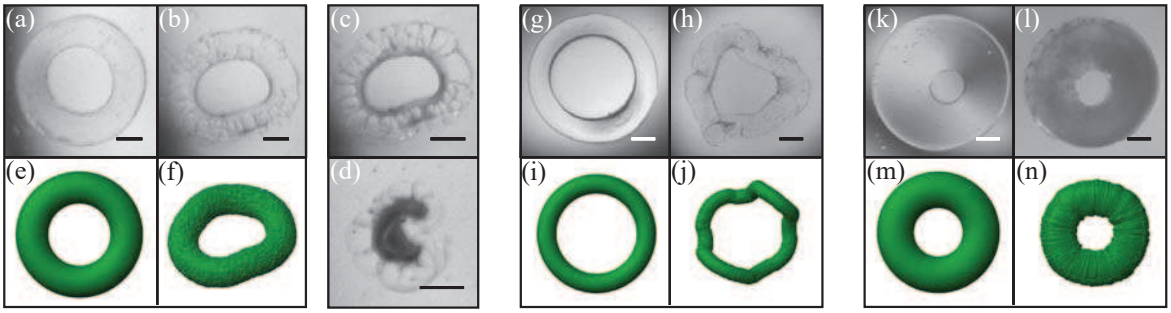

FIG. 3. Evolution of toroidal gels after rapid heating. The experimental image pairs (a,b), (g,h), and (k,l) are taken (a,g,k) 0s, (b) 104s, (h) 158s, and (l) 201s after heating. Pairs (e,f), (i,j), and (m,n) are simulations for gel shells; images on the left correspond to the initial state, while images on the right correspond to the final state. The initial aspect ratio of the tori are: (a) 3.3, (e) 3.0, (g) 4.8, (i) 5.3, (k) 1.7, and (m) 2.4. Images (c,d) correspond to the long-time evolution of the toroidal gel in (a,b). (c) is 3 min and (d) is 10 mins after the abrupt temperature change. Scale bars: 1mm.

tains a constant volume [17, 18]. The long-time patterns seen in our toroidal gels suggest that a similar situation occurs in our case and that the evolution we observe after rapid heating essentially happens at constant volume; this is supported by the observation that the time over which the toroid buckles is much shorter than the plateau period. Hence, after rapid heating, the gel is out of equilibrium with the solvent bath and is thus not constrained to maintain a constant osmotic pressure $\Pi_{\rm bath}$, but rather a constant volume. In this situation, a swollen gel is not allowed to change its total polymer volume fraction. However, since the swollen gel has been brought to a temperature above the LCST of pNIPAM, the homogeneously mixed state of the gel becomes unstable to separation into solvent-rich and solvent-poor regions. We then postulate that the shape transformation observed in experiment is due to this phase-separation at constant volume.

As the boundary of the torus already consists of a collapsed-polymer layer, we expect that the solvent-poor region grows from this layer inward into the bulk, in a manner akin to heterogeneous nucleation. Furthermore, since a gel is a contiguous medium, the interface between solvent-rich and solvent-poor regions is laminated. This interface frustrates the homogeneity of the polymer matrix and leads to a residual stress. We therefore expect that the phase-coexistent state adopted by the gel will tend to minimize this inhomogeneity. In the case of a sphere, the result is a solvent-poor skin of uniform thickness over the surface. The non-constant curvature of the toroidal surface, however, leads to a skin of *non-uniform* thickness. Since the toroidal gel has higher ring curvature on its interior surface than on its exterior, we expect that a thicker polymer layer will form near the axis of revolution of the torus, as illustrated in the rightmost schematic in Fig. 4(a). This is indeed seen in experiment and is particularly clear at long-times, where the solvent-poor skin has clearly thickened and appears opaque, as shown in Figs. 3(c,d).

To confirm our interpretations, we consider that, within the torus, a fraction f of the gel is solvent poor and undergoes a volume change relative to its initial volume, $u_p < 0$. The remaining fraction $(1-f)$ of the gel is solvent-rich and increases its volume by a factor $u_r > 0$. The total volume constraint yields a "lever rule" $fu_p + (1-f)u_r = 0$, which is a general feature in phase-separation with a conserved order parameter [19, 20]. Using the Flory-Rehner theory of polymer gels [12] and considering a cylindrical geometry, which amounts to neglecting ring curvature for now, we can determine equilibrium values for the strain u_r and u_p and the fraction f; from this, we confirm that phase-coexistent equilibria exist for temperatures T above the LCST at constant volume and that the polymer volume fraction for the solvent-poor region is much larger than that of the solvent-rich region [12]. We then incorporate perturbatively the toroid's ring curvature on the phase-coexistence and find that it is favorable for the solvent-poor region to be thicker near the axis of revolution of the torus and thinner away from the axis [12], further confirming our previous assertions. Interestingly, the resultant configuration is reminiscent of a bimetallic strip composed of two metals of differing thermal expansion coefficients that are laminated together, as illustrated in the leftmost schematic in Fig. 4(a); under heating, the strip bends, increasing curvature due to the torque that results from the differing thermal stresses in the two metals [21]. In our case, the laminated coexistent phases of the gel have a similar stress differential. We then focus on the ring-shape of the gel, ignore fine details of the cross-section, and develop a long-wavelength elastic model where the polymer matrix in the two laminated coexistent gel regions are each at *fixed polymer volume fractions*. Within this coarse-grained view of the gel, the net compressive stress, σ, exerted by the outer, solvent-poor shell on the inner, solvent-rich region is: $\sigma = E(u_r - u_p)$, where E is the gel's effective Young's modulus.

To describe buckling, we balance the stress σ against

the rigidity of the torus. In general, toroidal bending is described by three-dimensional elasticity. However, in our simplified model we treat the torus as an elastic rod defined by a circular centerline of length L. This centerline is characterized at each point by its curvature κ and torsion τ, which are determined by the rotation rate of the Frenet-Serret frame; see inset in Fig. 4(b). We consider an effective inextensible rod elastic free-energy H [2], in which the centerline degrees of freedom are encoded in changes in curvature $\Delta\kappa$ and changes in torsion $\Delta\tau$ at fixed length:

$$H = \int_0^L \mathrm{d}s \left(\frac{1}{2} B \, \Delta\kappa^2 + \frac{1}{2} C \, \Delta\tau^2 + \Delta\kappa \, \hat{\mathbf{b}} \cdot \mathbf{M} \right). \quad (1)$$

The first two terms in Eq. (1) represent a rod with Hookean response to bending (and bending rigidity B) and twisting (and torsional rigidity C). The third term in Eq. (1) is associated to the swelling torque $\mathbf{M}$ acting on the centerline. This model becomes strictly applicable in the limit $\xi \gg 1$. However, since the extensile rigidity remains much larger than the bending or torsional rigidities for significantly smaller ξ [22], it still applies down to the experimental values of ξ where buckling is observed.

Right away, we see that our simple model indicates that the torus experiences swelling stresses that act to increase the ring curvature, reminiscent of the thermal stresses that bend bimetallic strips. Owing to the relatively high energy cost of length changes, the torus is unable to attain a uniformly increased curvature whilst remaining planar, because any deformation that preserves both the length and winding number of a closed planar loop also leaves the integrated curvature for that loop unchanged [23]. To overcome this, the torus buckles out of the plane, which is what we observe experimentally.

To find the buckling threshold and modes, we perform a linear stability analysis [12, 24] of Eq. (1). This analysis depends on two dimensionless numbers: the rigidity ratio C/B and the stress ratio $M/(B\kappa)$, where $M \equiv |\mathbf{M}|$. We find that the torus is unstable to buckling above a threshold value of $M/(B\kappa)$ at fixed C/B, as shown in Fig. 4(b). This is seen in experiments, where tori with $\xi \lesssim 3$ do not buckle; see Fig. 3(k,l) for a representative example. Note that "Pringling" is the first of the buckling modes that is accessible upon increasing $M/(B\kappa)$ at fixed C/B. For even larger $M/(B\kappa)$, higher modes become unstable [Fig. 4(b)].

Let us now estimate the quantities in Eq. (1) and further compare to experiments. The swelling torque $\mathbf{M} = -fx\pi a^2\sigma\,\hat{\mathbf{b}}$ can be estimated as the cross-product of the lever arm $fx\,\hat{\mathbf{n}}$ with force $\pi a^2\sigma\,\hat{\mathbf{t}}$. Here, f is a good approximation of the fraction of the cross-sectional area occupied by the solvent-poor region, and x is the center-of-area of the surface skin within the cross-section, which measures the imbalance of skin thickness due to surface curvature. Note that $x > 0$ because the shell is thicker closer to the axis of revolution of the torus. To

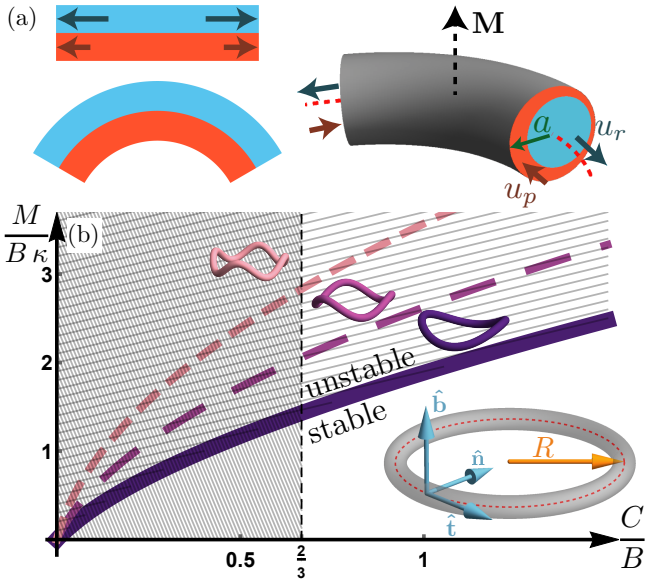

FIG. 4. (a) Schematic of a bimetallic strip before (top left) and after (bottom left) heating. A slice through the cross-section of a phase-separated toroid is shown on the right with centerline (dashed red), cross-sectional radius a, polarized arrangement of solvent-rich (blue) and solvent-poor (orange) regions with corresponding strains u_r and u_p, and the swelling moment $\mathbf{M}$. (b) Prediction of instability from linear stability analysis in terms of dimensionless measures of the swelling moment, $M/(B\,\kappa)$, and the ring rigidity, C/B. The inset schematically shows the Frenet-Serret frame in an unperturbed ring, as well as the "Pringling" and the next-two-lowest modes. Note that for uniform incompressible tori with a circular cross-section, elasticity theory dictates that $C/B \approx 2/3$.

estimate the rigidities we consider that a uniform rod of circular cross-section radius a has $B \approx \frac{1}{4}\pi a^4 E$ and $C/B \approx (1+\nu)^{-1}$, with ν the Poisson ratio. Crucially, since the gel is in the plateau period where the volume remains constant, we may regard it as *rubber-like* and hence incompressible; thus we take $\nu \approx 1/2$ and $C/B \approx 2/3$. We then find that $M/(B\kappa) \approx 4f\xi$, where we have used that $x \approx a$, due to the highly polymer-dense region at the toroidal surface, and that $|u_p| \approx 1$, since this region contains very little solvent [12]. Theoretically, the buckling threshold for $C/B = 2/3$ is $M/(B\kappa) \approx 1.4$. Considering that buckling is seen above $\xi \approx 3$, this implies that $f \approx 0.1$. We can test this expectation by considering the ratio of deswollen to swollen gel volumes in the *quasistatic* experiments (see Fig. 2); in all cases, we obtain $f \approx 0.1$, consistent with the theoretical expectations. Moreover, as $M/(B\kappa) \sim \xi$, the theoretical predictions of the buckling modes shown in Fig. 4(b) relate well to the experiments. Specifically, increasing ξ in the experiments results in a transition from tori that are stable against buckling to ones that "Pringle," and subsequently to tori that deform via more complicated shapes, which

are reminiscent of the higher buckling modes predicted by the linear-stability analysis.

To further confirm that a swollen interior surrounded by a dense shell that is thicker near the axis of revolution results in buckling, we perform DPD simulations of toroidal shells having a nearly constant volume. Since we model the toroidal shell by a 4-coordinated mesh of harmonic bonds [12], the curvature of the shell ensures that the effective rigidity of the portion closer to the axis of revolution is greater than the portion away from the axis, simulating the variable thickness observed in experiments. Remarkably, the simulations reproduce the "Pringle$^{\mathrm{TM}}$"-like shape seen experimentally, as shown for a torus with $\xi = 3.0$ in Figs. 3(e,f). Furthermore, the data can be fit to the hyperbolic paraboloid shape characteristic of Pringles [12]. Our simulations confirm that buckling is indeed related to the heterogeneous structure of our gels, in which a solvent-poor layer is forced to coexist with a solvent-rich bulk, and that in the process the volume of the gel remains essentially constant. We also note that we also find modes other than "Pringling." These are seen for higher values of ξ; an example is shown in Figs. 3(i,j), which compares well with the experimental result shown in Figs. 3(g,h). In addition, for sufficiently small ξ, no buckling is observed, consistent also with our experiments and theory, and buckling occurs only for $\xi \gtrsim 3$, also consistent with our experimental findings.

We have shown that rapidly heated tori composed of polymer gel can undergo constrained phase separation to form solvent-rich and solvent-poor regions and that the polarized arrangement of these regions within the torus can result in out-of-plane deformations. Our theoretical analysis also predicts that thin, curved pNIPAM gel rods would buckle when $f \gtrsim 0.35\,\xi^{-1}$, where in general f is the volume fraction of solvent-poor gel and $\xi^{-1} = \kappa a$ is the product of rod curvature κ and the tube radius. While the shapes attained in our experiments are typical for rings that buckle due to mechanical instability, we emphasize that our results are entirely due to a *thermodynamic instability*. Thus, our work is suggestive of an "extreme thermodynamics" where shape actuation is achieved by passage through a phase transition.

This work was supported by the National Science Foundation (DMR-1609841, DMR-1207026, DMR-1255288). The work of PMG was also performed in part at the Aspen Center for Physics (NSF PHY-1607611). SVN is thankful to the NSF Graduate Research Fellowship program (DGE-1650044).

---

* These two authors contributed equally

[1] P. M. Reis, H. M. Jaeger, and M. van Hecke, Extreme Mech. Lett. **5**, 25 (2015).
[2] L. Landau, E. Lifshitz, A. Kosevich, and L. Pitaevskiĭ, *Theory of Elasticity* (Butterworth-Heinemann, New York, 1986).
[3] M. Shibayama and T. Tanaka, "Volume phase transition and related phenomena of polymer gels," in *Responsive Gels: Volume Transitions I*, edited by K. Dušek (Springer, Berlin, Heidelberg, 1993) pp. 1–62.
[4] P. J. Flory, *Principles of Polymer Chemistry* (Cornell University Press, Ithaca, 1953).
[5] M. Arifuzzaman, Z. L. Wu, R. Takahashi, T. Kurokawa, T. Nakajima, and J. P. Gong, Macromolecules **46**, 9083 (2013).
[6] V. Trujillo, J. Kim, and R. C. Hayward, Soft Matter **4**, 564 (2008).
[7] D. Breid and A. J. Crosby, Soft Matter **7**, 4490 (2011).
[8] E. Hohlfeld and L. Mahadevan, Phys. Rev. Lett. **106**, 105702 (2011).
[9] M. Guvendiren, S. Yang, and J. A. Burdick, Adv. Funct. Mater. **19**, 3038 (2009).
[10] G. Stoychev, S. Zakharchenko, S. Turcaud, J. W. C. Dunlop, and L. Ionov, ACS Nano **6**, 3925 (2012).
[11] S. Hirotsu, "Coexistence of phases and the nature of first-order phase transition in poly-n-isopropylacrylamide gels," in *Responsive Gels: Volume Transitions II*, edited by K. Dušek (Springer, Berlin, Heidelberg, 1993) pp. 1–26.
[12] See Supplemental Material at [URL will be inserted by publisher] for details on (i) the generation of toroidal polymer gels and the quasistatic deswelling experiments, (ii) the DPD cmputer simulations, (iii) the fit of the simulation Pringle-like shape to a hyperbolic paraboloid, (iii) the phase coexistence equilibrium at constant volume for cylindrical polymer gels, (iv) the role of ring curvature on this phase coexistence, and (v) the linear stability analysis of the ring model.
[13] Y.-W. Chang, A. A. Fragkopoulos, S. M. Marquez, H. D. Kim, T. E. Angelini, and A. Fernández-Nieves, New J. Phys. **17**, 033017 (2015).
[14] E. Pairam, H. Le, and A. Fernández-Nieves, Phys. Rev. E. **90**, 021002 (2014).
[15] H. G. Schild, Prog. Polym. Sci. **17**, 163 (1992).
[16] E. Sato Matsuo and T. Tanaka, J. Chem. Phys. **89**, 1695 (1988).
[17] R. Yoshida, K. Sakai, T. Okano, Y. Sakurai, B. You Han, and K. Sung Wan, J Biomater. Sci. Polym. Ed. **3**, 155 (1992).
[18] T. Okano, Y. H. Bae, H. Jacobs, and S. W. Kim, J. Control. Release **11**, 255 (1990).
[19] P. M. Chaikin and T. C. Lubensky, *Principles of Condensed Matter Physics* (Cambridge University Press, Cambridge, 1995).
[20] H. B. Callen, *Thermodynamics and an Introduction to Thermostatistics* (Wiley, 1985).
[21] S. Timoshenko, J. Opt. Soc. Am. **11**, 233 (1925).
[22] M. S. Dimitriyev, *Function through form in soft matter: the influence of bounded geometries in heated gels and fluctuating proteins*, Ph.D. thesis, Georgia Institute of Technology, School of Physics (2017).
[23] A. Pressley, *Elementary differential geometry* (Springer-Verlag, London, 2010).
[24] B. Audoly and Y. Pomeau, *Elasticity and Geometry: From hair curls to the non-linear response of shells* (OUP Oxford, 2010).

Supplementary Information

May 18, 2018

1 Generation of toroidal hydrogels and details of the quasistatic deswelling experiments

We fabricate toroidal gels by first forming toroidal droplets of a precursor solution consisting 5% NIPAM, 0.2% crosslinker bis-acrylamide, 0.2% (w/v) photo-initiator Irgacure 2959, and 94.6% deionized water, inside a yield-stress material made of a mixture of Dow Corning® 9041 silicone elastomer blend and 10cst silicone oil [1]. The process consists of injecting the precursor fluid through a needle into a rotating bath containing the yield-stress material. At sufficiently high rotation speeds, the stresses involved exceed the yield stress, and we can successfully generate a curved jet that closes onto itself to form a toroidal droplet. Once made, the shape is stabilized by the elasticity of the yield-stress material [2]. We induce polymerization of the precursor fluid by illuminating the sample with UV-light while keeping it over an ice bath, which assists with heat dissipation and prevents macro-phase separation of pNIPAM aggregates during polymerization. The resultant toroidal gel is removed from the yield-stress material by repeated cleaning with alcohol and water, and maintained in deionized water.

Quasistatic deswelling experiments are performed by transferring a fully swollen gel into a water bath that is placed over a platform with temperature control capability; the temperature of the bath is measured using a thermocouple of sensitivity ± 0.1 °C. The volume and shape transition of the toroidal gel are monitored using a CCD camera. To ensure quasistatic deswelling, we change the temperature at a rate ≤ 0.4 °C/hour. Alternatively, we change the temperature in small steps, waiting as needed after each step until no size change is detected; the results we observe are identical. We also emphasize that the deswelling behavior is fully reversible.

2 Simulation information

In our computational model, we utilized dissipative particle dynamics (DPD), a particle-based mesoscopic simulation technique, whose soft potentials and pairwise forces preserve local hydrodynamics while allowing for simulations with longer length and time scales [3, 4, 5]. The governing dynamics between beads in DPD are set by three main forces, $\mathbf{F} = \sum_{j \neq i} \mathbf{F_{ij}^C} + \mathbf{F_{ij}^D} + \mathbf{F_{ij}^R}$. The conservative force $\mathbf{F_{ij}^C} = a_{ij}\, w(r_{ij})\, \hat{\mathbf{r}}_{\mathbf{ij}}$ leads to excluded volume. In this expression, a_{ij} is the repulsion parameter between beads i and j, and $w(r_{ij}) = 1 - \hat{r}_{ij}$ is a weighing function, where $\hat{r}_{ij} = r_{ij}/r_C$, with $r_{ij} = |\mathbf{r_i} - \mathbf{r_j}|$ and r_C the cut-off distance of the excluded volume potential. The dissipative force $\mathbf{F_{ij}^D} = -\gamma\, w^2(r_{ij})\, (\hat{\mathbf{r}}_{\mathbf{ij}} \cdot \mathbf{v_{ij}})\, \hat{\mathbf{r}}_{\mathbf{ij}}$, with $\mathbf{v_{ij}}$ the difference in velocity between beads i and j, accounts for viscous interactions, while the random force $\mathbf{F_{ij}^R} = \sigma\, w(r_{ij})\, \xi_{ij} \cdot (\Delta t)^{-1/2}\, \hat{\mathbf{r}}_{\mathbf{ij}}$ represents the effect of thermal fluctuations. In the expression for $\mathbf{F_{ij}^R}$, ξ_{ij} is a standard normal variable with zero mean and Δt is the time-step of the velocity verlet algorithm; the time-step dependence is required to guarantee that Brownian motion, which is characterized by a magnitude of the displacement-step that scales with the square-root of the time-step, is recovered upon integration. The random and dissipative forces are related by $\sigma^2 = 2\,\gamma\, k_B\, T$, with k_B the Boltzmann constant and T the temperature, due to the fluctuation-dissipation theorem. For our simulations, we set $a_{ij} = 25$, $r_C = 1$, $\gamma = 4.5$, $k_B\, T = 1$, and $\rho = 3$ (all dimensional parameters are given in DPD units) [3].

We developed two different toroidal gel models to describe the slow and rapid heating rates in the experiments. For slow heating rates, we represent the toroidal polymer network using randomly connected

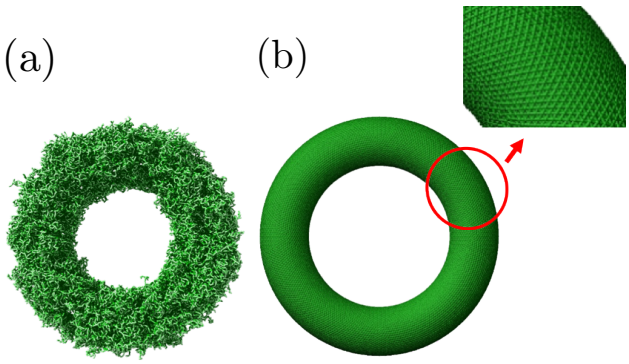

Figure S.1: (a) Example image of a toroidal polymer network used to model quasistatic deswelling. (b) Illustration of a toroidal mesh with close-up, used to model the rapid heating rate experiments.

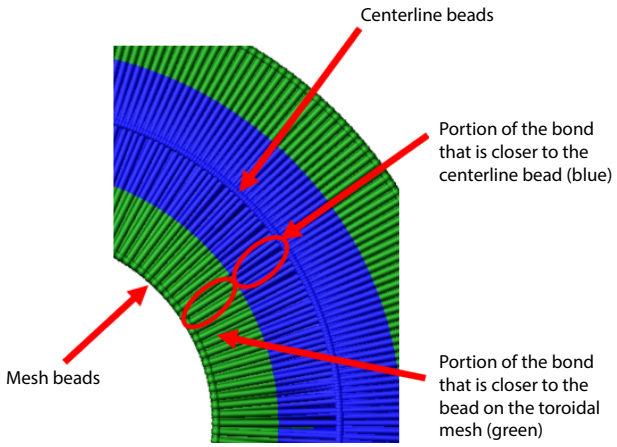

Figure S.2: Cross-sectional view of toroids for rapid heating simulations. The beads in the toroidal mesh and centerline beads are shown in green and blue, respectively. Each mesh-centerline bond is represented with a half-green and a half-blue color scheme for illustration purposes.

bead-spring chains. In this approach, the flexible chains are composed of beads connected by a harmonic potential given by $U_{\text{bond}} = k_{\text{bond}}\,(r - r_{\text{eq}})^2$ and a bending potential given by $U_{\text{bend}} = k_{\text{bend}}\,(1 + \cos\theta)$. Here, k_{bond} is the bond stiffness, r_{eq} is the equilibrium separation length between beads, k_{bend} is the bending stiffness and θ is the angle between two polymer bonds sharing a common bead. In our simulations, we set $k_{\text{bond}} = 35$, $r_{\text{eq}} = 0.6$, and $k_{\text{bend}} = 1$. To construct our toroidal gel network, we randomly distribute crosslink points in a $60 \times 60 \times 60$ simulation domain and then connect them with nearby neighbors via flexible chains using a connectivity of 6. The toroidal geometries are cut out from the corresponding cubic networks and placed in a $100 \times 100 \times 100$ simulation domain filled with a viscous solvent with density $\rho = 3$ represented by DPD beads. Deswelling of toroidal gels is achieved by varying the gel-solvent repulsion parameter a_{N-S} [6]. Theta-solvent conditions correspond to $a_{N-S} = 25$. Lower values of a_{N-S} correspond to good solvent and higher values correspond to poor solvent conditions. To model the collapse of the toroidal gel, we start at theta-solvent conditions and incrementally decrease the solvency until we reach $a_{N-S} = 35$. Figure S.1a shows a snapshot of our toroidal network in theta-solvent conditions. The swelling kinetics of our random polymer network model, in the case of spherical geometries, agrees well with Tanaka's theory for the swelling of gels [6, 7].

Due to computational constraints, our gel model cannot be directly used to model the rapid heating rate experiments with macroscopic gels, which is characterized by the formation of a dense, stiff skin at the gel-solvent interface. To model the effects of the stiff gel skin which forms in these cases, we use a simplified

model that is composed of a toroidal shell constructed using a tetrahedral mesh with an average spacing of $\sim$0.35, as shown in Fig. S.1b. Nodes in the mesh are connected by harmonic bonds. To mimic the effect of the gel heating rate, we arrange beads along the toroidal centerline and connect them to the beads forming the shell. Mesh-centerline bonds are shown in the cross-sectional view in Fig. S.2, where half of each bond is colored in blue (parts closer to the centerline bead) and the other half is colored in green (portion of the bond closer to the mesh bead). The initial equilibrium bond length for the mesh-centerline bonds was set to 5. The harmonic bonds in the shell have stiffness $k = 500$, while the mesh-centerline harmonic bonds have stiffness $k = 100$. Note that we do not impose a DPD repulsion between the beads in the mesh, as this would have effects on the mesh properties that we want to avoid. The repulsion between mesh-solvent beads is $a_{M-S} = 100$. The density of the fluid is $\rho = 3$, yielding an average spacing between solvent beads of about 0.7. The smaller spacing between beads in the mesh and the relatively large repulsion between mesh-solvent beads ensures that solvent particles which are initially inside of the toroidal mesh remain trapped during the rapid heating process. To model this rapid heating, we instantaneously decrease the mesh-centerline equilibrium bond length from 5 to 3. The final bond length is selected based on the numerical stability of the shell model.

3 Comparison between simulation and Pringle$^{\mathrm{TM}}$ shape

We compare the simulation results to the Pringle$^{\mathrm{TM}}$ shape predicted by our elastic ring model by fitting the simulated centerline, an example of which is shown in Fig. S.3(a) below, to a ring that lies on a hyperbolic paraboloid $z = q\,(x^2 - y^2)$, which, in polar coordinates is given by

$$(x,\, y,\, z) = R\left(\cos(\theta+\delta),\, \sin(\theta+\delta),\, q\,R\,\cos(2\theta+\delta)\right), \tag{1}$$

where R is the radius of the projection of the ring onto the xy-plane, δ is a phase-offset, and q determines the amplitude of the out-of-plane component of the buckled ring. To perform this fit, we first translate and rotate the simulated points such that (i) the origin $x, y, z = 0$ coincides with their center-of-mass and (ii) the z-axis aligns with the principle axis corresponding to their smallest dimension. Next, we fit the projected ring radius R against the projection of the simulated centerline to the xy-plane. Using this value of R, we fit $q\,R^2\,\cos(2\theta+\delta)$ to the z-axis projection of the centerline, as shown in Fig. S.3(b), obtaining values of $A = q\,R^2$ and the phase-offset δ. For the specific case shown in this figure, we obtain an amplitude of $A/R \approx 0.068$ and $\delta \approx 0.242$ radians. As evidenced by Figs. S.3(b,c), the buckled shape is well-approximated by a ring on a hyperbolic paraboloid, i.e., the Pringle$^{\mathrm{TM}}$ shape.

We note that since we lack a three-dimensional view of the toroids in the experiments, we cannot provide a similar quantitative analysis of the observed, buckled Pringle-like shape.

4 Phase coexistence in a gel rod

To address the phase-coexistence between solvent-poor (deswollen) shell and solvent-rich (swollen) interior, we approximate the toroid by a cylinder with identified end-caps; the toroid's ring curvature lifts the cylinder's polar symmetry. In the absence of ring curvature, symmetry dictates that the cylinder can only change its length by a stretching factor Λ_ℓ, the radius of the solvent-rich region by a factor Λ_t, and the thickness of the solvent-poor region by Λ_n. This situation is illustrated in Fig. S.4. The total free-energy, in the reference space $\mathcal{R}$, is given by

$$\begin{aligned}\frac{F}{\pi\,a^2} =& (1-f)\left[\frac{1}{2}\,\mu_0\,\left(\Lambda_\ell^2 + 2\,\frac{\phi_0}{\phi_r\,\Lambda_\ell}\right) + \mathcal{F}(\phi_r)\right] \\ &+ f\,\left[\frac{1}{2}\,\mu_0\,\left(\Lambda_\ell^2 + \phi_0\,\frac{\phi_p^{-2}+\phi_r^{-2}}{\phi_r^{-1}\,\Lambda_\ell}\right) + \mathcal{F}(\phi_p)\right] \\ &+ p\,\left[(1-f)\frac{\phi_0}{\phi_r} + f\,\frac{\phi_0}{\phi_p} - 1\right]\end{aligned} \tag{2}$$

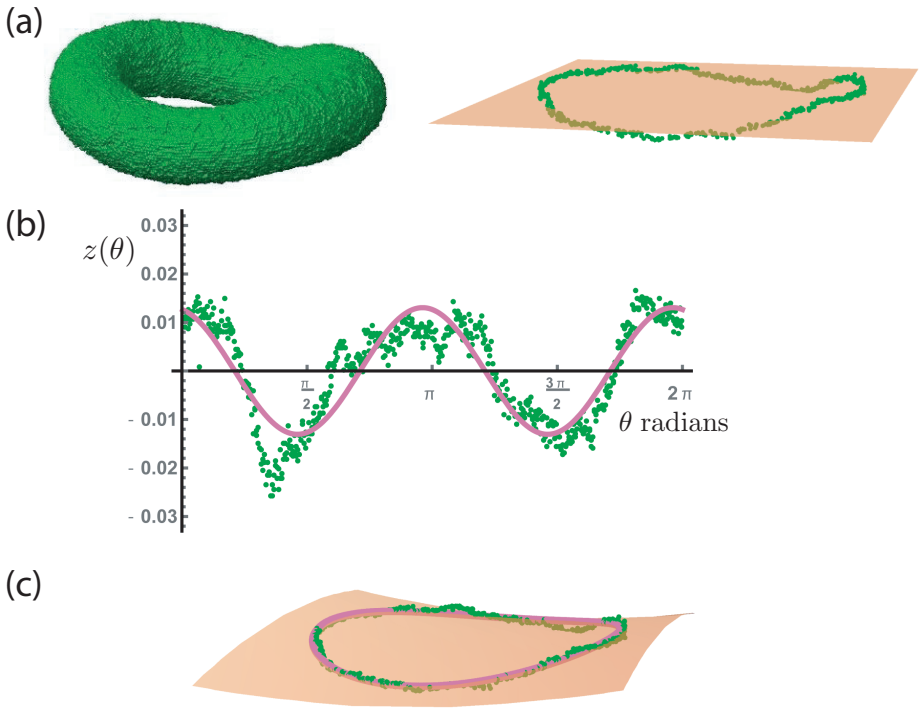

Figure S.3: (a) Buckled shape from DPD simulation, with extracted centerline (right) and xy-plane. (b) Height of the ring as measured along the z-axis of (a), together with a fit to $A\cos(2\theta+\delta)$, where $A = q\,R^2$ is the amplitude of the ring deformation and δ is a phase offset, accounting for the choice orientation in the xy-plane; in this example, we find $\delta \approx 0.242$ (radians) and $A/R \approx 0.068$. (c) Overlay of the data with the fit ring on a portion of the corresponding hyperbolic paraboloid surface.

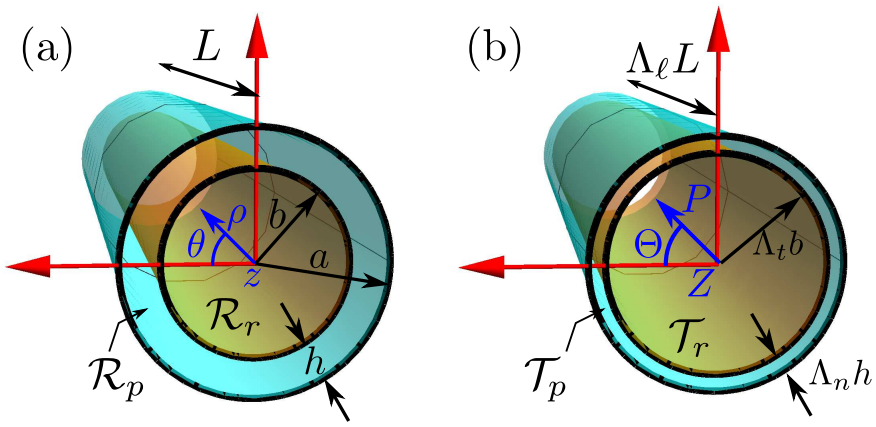

Figure S.4: Schematic of phase-separated cylinder (a) before and (b) after deformation along with cylindrical coordinates. In the reference configuration (a), L is the length of the cylinder, b is the radius of the solvent-rich region, h is the thickness of the solvent-poor skin, $\mathcal{R}_r$ is the solvent-rich region, $\mathcal{R}_p$ is the solvent-poor region. $\mathcal{T}_r$ is the solvent-rich region and $\mathcal{T}_p$ is the solvent-poor region in the target configuration (b).

where μ_0 is the shear rigidity of the gel before phase-separation, with polymer volume fraction ϕ_0; after phase-separation, the gel has a solvent-poor shell with polymer volume fraction $\phi_p^{-1} = \Lambda_n \Lambda_t \Lambda_\ell \phi_0^{-1}$ and solvent-rich interior with polymer volume fraction $\phi_r^{-1} = \Lambda_t^2 \Lambda_\ell \phi_0^{-1}$. The parameter p is a Lagrange multiplier that enforces the constant volume condition. The mixing free energy density $\mathcal{F}$ is modeled by the Flory-Rehner theory [8, 9]; for description of the continuum approach, see e.g. [10]. In order to describe the first-order phase transition that occurs in the neutral polyNIPAM gels, the Flory-Rehner theory is extended via a virial expansion of the osmotic pressure [11], leading to a volume fraction-dependent Flory parameter, which may be approximated as

$$\chi(\phi, T) \approx \chi_1(T) + \chi_2\, \phi \tag{3}$$

where χ_2 is typically taken to be fixed by experiment with a value $\chi_2 > 1/3$ [12]; temperature sets the value of χ_1 which determines the swelling state of the gel. Minimizing the total free-energy Eq.2 with respect to ϕ_r, ϕ_p, Λ_ℓ gives stress-balance conditions; minimization with respect to f yields a chemical potential-balance condition between the two phases; minimization with respect to p yields the "lever rule"

$$f = \frac{\phi_r^{-1} - \phi_0^{-1}}{\phi_r^{-1} - \phi_p^{-1}} \tag{4}$$

which is simply a consequence of mass and volume conservation and thus holds for systems undergoing phase separation into two distinct phases [13]. Note that in the manuscript, in order to clarify the form of our elastic model, we introduce the strains u_r and u_p where

$$u_r \equiv \frac{\phi_0 - \phi_r}{\phi_r}; \;\; u_p \equiv \frac{\phi_0 - \phi_p}{\phi_p} \tag{5}$$

which allows the lever rule Eq. 4 to be recast as

$$f = \frac{u_r}{u_r - u_p}\,. \tag{6}$$

Fig. S.5 outlines the theoretical predictions for the equilibrium state of a long cylindrical gel, with fixed solvent and polymer mass, as a function of Flory parameter χ_1, which is a proxy for temperature. In particular, we focus on gels that contain a much greater mass of solvent than polymer, characterized by a low single-phase polymer volume fraction ϕ_0, and consider three cases of polymer dilution: $\phi_0 = 0.01$, 0.015, and 0.02. We use representative values $\mu_0 = 10^{-4} k_B T/v$ and $\chi_2 = 0.56$ (see [12]). Equilibrium values of the polymer volume fraction are shown in Fig. S.5(a), where we note that for small χ_1, there is a single

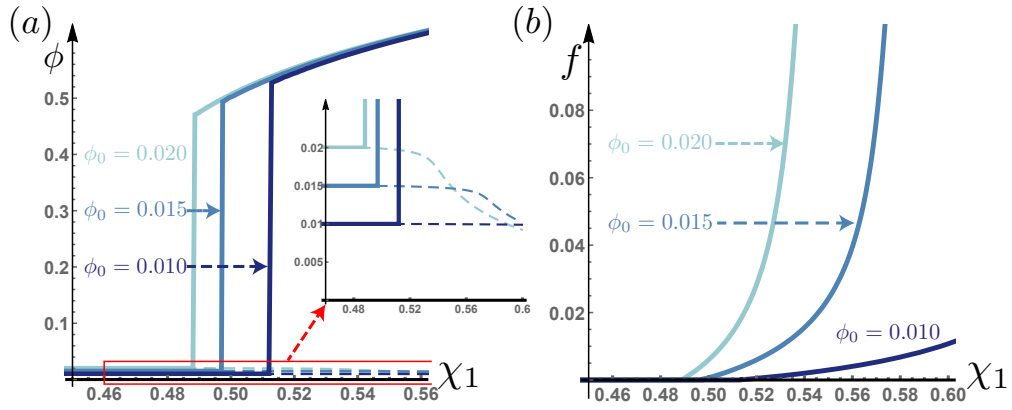

Figure S.5: (a) Values of solvent-poor volume fraction ϕ_p (solid) and solvent-rich volume fraction ϕ_r (dashed) after constrained phase separation are shown as a function of χ_1, with inset highlighting the low-ϕ regime, showing variation in the solvent-rich volume fraction ϕ_r. (b) Fraction f of solvent-poor phase in the reference state is shown as a function of χ_1.

equilibrium volume fraction, given by ϕ_0, and for larger χ_1, the gel phase-separates and the equilibrium state is characterized by coexistent solvent-rich and solvent-poor phases with volume fractions ϕ_r (dashed curve) and ϕ_p (solid curve), respectively. Thus, the gel undergoes a first-order deswelling phase transition resulting in the large, discontinuous jump in ϕ_p from ϕ_0. We find, however, that the solvent-rich region is characterized by a volume fraction ϕ_r that decreases continuously from ϕ_0; this is emphasized in the inset of Fig. S.5(a), which focuses on a smaller range of volume-fraction and a larger range of χ_1 to highlight the variation in ϕ_r. Note that for more dilute gels (lower ϕ_0), the phase-separation transition occurs at higher χ_1 and variation of ϕ_r from ϕ_0 is diminished. We emphasize, though, that there is still a variation in ϕ_r from ϕ_0 for the case of $\phi_0 = 0.01$; this variation is apparent after zooming in appropriately.

To better understand the behavior of the phase-separated volume fractions, refer to Fig. S.5(b), which shows the fraction f of the cylinder that is occupied by solvent-poor gel. Since the solvent-poor region grows from the deswollen boundary of the cylinder, rather than the core, where it would need to grow from a critical nucleus, f grows continuously from 0. Within this picture, the solvent-poor region obtains more polymer mass from the solvent-rich region in order to grow, decreasing the polymer volume fraction ϕ_r of the solvent-rich region; this decrease is continuous because the growth of f is continuous. The observed increase in the rate of change of ϕ_r in the inset of Fig. S.5(a) and of f in Fig. S.5(b) with larger values of χ_1 can be explained by recalling that phase-separation in gels is different from phase-separation in fluids due to the presence of shear rigidity: the formation of separate phases results in an inhomogeneous strain of the polymer network, resulting in a free-energy cost, which limits the growth of separate phases. However, since the elastic modulus μ_0 is independent of χ_1, for sufficiently large χ_1 (sufficiently poor solvent), the portion of the free-energy density due to solvent-polymer mixing overwhelms the elastic part of the free-energy density. As a result, the limiting role of polymer network rigidity in the growth of the solvent-poor phase becomes progressively less important, leading to the increased rate of change of f with χ_1, and the associated increased change in ϕ_r.

Finally, the shift of the transition value of χ_1 to lower values with increasing ϕ_0 is due to the correspondingly higher energy density of solvent-polymer mixing with increasing ϕ_0: for increasing values of ϕ_0 (in the regime of $\phi_0 \ll 0.5$), there is increasing contact between polymer and solvent molecules (with maximum mixing at $\phi_0 = 0.5$). Thus, the effect of solvent-quality change is greater, resulting in a lower transition value of χ_1, as well as a greater rate of change in ϕ_r and f with increasing χ_1.

We also emphasize that our model holds in the low f limit, which is our case, since for larger values of f, we would not be able to treat the skin as an elastic shell and would have to resort to solving the continuum equilibrium equations. (We note that $f \approx 0.1$ is consistent with the magnitude predicted by our cylinder model.)

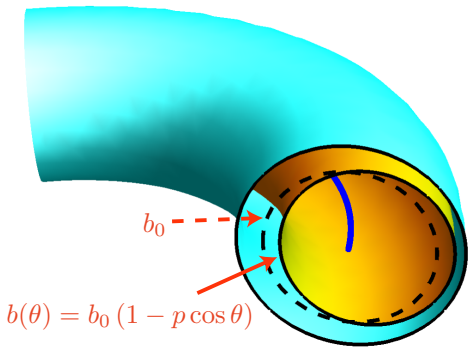

Figure S.6: Adding curvature to the gel cylinder necessitates a *polarization* p of the solvent distribution, described as a displacement of the interface between coexistent regions as shown above.

5 Phase separation in tori: introducing ring curvature as a perturbative correction

To determine the effect of the toroid's ring curvature on the phase coexistence, we start with the above cylindrical core-shell model and add the effect of ring curvature $\kappa = 1/R$ *perturbatively*. Note that adding the ring curvature lifts the axial symmetry of the cylinder. As a result, we may no longer assume that the solvent-poor skin has as uniform thickness as a function of the angular coordinate θ; in general, the thickness varies as a function of θ. Equivalently, the position of the interface between solvent-rich and solvent-poor regions is no longer at a fixed radius, viz. $\rho = b$ in the polar coordinates of Fig. S.5. In general, the interface position may be decomposed in Fourier modes as $b(\theta) = b_0 + b_1 \exp i\theta + b_2 \exp 2i\theta + \ldots$, where b_n denotes the amplitude of the n^{th} mode. However, in analogy with the multipole expansion of the scalar potential in electrostatics, the expansion of $b(\theta)$ can be expressed in terms of multipole moments; for example, b_0 characterizes a scalar "charge," b_1 a vector "polarization," b_2 a rank-2 tensor "quadrupole," etc. Note that the curvature is a vector quantity $\boldsymbol{\kappa} = \kappa\hat{\mathbf{b}}$, where $\hat{\mathbf{b}}$ is the centerline's binormal direction. Therefore, the lowest-order term in the free-energy of the gel ring that incorporates coupling between curvature and interface shape $b(\theta)$ is a coupling between the curvature vector $\boldsymbol{\kappa}$ and the vector part of the interface shape, i.e. the polarization $\mathbf{p}$. Since the toroid is symmetric with respect to a reflection about its plane, spanned by the tangent vector $\hat{\mathbf{t}}$ and normal vector $\hat{\mathbf{n}}$, the coupling between $\mathbf{p}$ and $\boldsymbol{\kappa}$ in the free-energy must maintain this symmetry. Thus, the coupling is proportional to the triple product, $(\mathbf{p} \times \hat{\mathbf{t}}) \cdot \boldsymbol{\kappa} = -\kappa\hat{\mathbf{n}} \cdot \mathbf{p}$. As the curvature-polarization coupling term above is the leading-order coupling of polarization to the ring curvature, the remainder of the free-energy is a function of the magnitude $|\mathbf{p}|$ alone. The equilibrium orientation of the polarization $\mathbf{p}$, as found by minimizing the free-energy, must therefore point toward the axis of revolution, i.e. in the $\hat{\mathbf{n}}$ direction, or away, i.e. in the $-\hat{\mathbf{n}}$ direction; such a configuration is shown in Fig. S.6. This allows us to set $\mathbf{p} = -p\hat{\mathbf{n}}$. Additionally, the same symmetry argument informs coupling of the polarization to the bending strain, proportional to the change in curvature $\Delta\boldsymbol{\kappa}$. Therefore, we conclude that the swelling torque $\mathbf{M}$ that is described in the manuscript is proportional to the polarization: $|\mathbf{M}| \propto p$.

In order to show that the ring curvature of the toroid leads to a solvent distribution where the polymer-dense region is near the axis of revolution of the toroid, i.e. where $p > 0$, we consider the change in the free energy of the cylinder in phase-coexistent equilibrium Eq. 2 due to the addition of a ring curvature κ and a polarized solvent distribution with polarization p. As the addition of these terms lifts the axial symmetry of the cylinder, the homogeneous deformations described by Λ_t, Λ_ℓ, and Λ_n generally acquire inhomogeneous, anisotropic corrections. These corrections are described by a strain tensor ϵ, the scale of which is set by the small parameters κ and p. Thus, we are able to consider a separation of scales: the phase-separation, resulting in the solvent-rich core surrounded by the solvent-poor shell, is described by the large deformation matrix elements $\{\Lambda_t, \Lambda_\ell, \Lambda_n\}$ and can be approximated by the values obtained in the cylindrical limit of the gel; the small inhomogeneous strain corrections ϵ can then be worked out in the linear elastic regime. Following this analysis (see [14]), we find that $\mathbf{p}$ aligns in the direction of $\hat{\mathbf{t}} \times \boldsymbol{\kappa} = -\kappa\hat{\mathbf{n}}$. This confirms the

intuition developed in quasistatic deswelling experiments, where the stress of maintaining coexistent phases is minimized if the deswollen phase is located closer to the axis of revolution and the swollen phase is pushed in the opposite direction.

6 Linear stability analysis of the ring model

To determine the stability of the planar ring, we parametrize the centerline as

$$\boldsymbol{\gamma'}(s) = R\left(\cos\frac{s}{R}, \sin\frac{s}{R}, 0\right) + \zeta\left(\frac{s}{R}\right)\hat{\mathbf{b}} = \boldsymbol{\gamma}(s) + \zeta\left(\frac{s}{R}\right)\hat{\mathbf{b}} \tag{7}$$

where ζ is a small out-of-plane deflection and $\hat{\mathbf{b}} = (0,0,1)$. The resulting Frenet-Serret frame is given by

$$\begin{aligned}
\hat{\mathbf{t}}' &= \frac{\partial_s \boldsymbol{\gamma'}}{|\partial_s \boldsymbol{\gamma'}|} \approx \left(1 - \frac{1}{2}(\partial_s\zeta)^2\right)\hat{\mathbf{t}} + \partial_s\zeta\,\hat{\mathbf{b}} \\
\hat{\mathbf{n}}' &= \frac{\partial_s \hat{\mathbf{t}}'}{|\partial_s \hat{\mathbf{t}}'|} \approx -(\partial_s\zeta)(\partial_{ss}\zeta)\,\hat{\mathbf{t}} + \left(1 - \frac{1}{2}(\partial_{ss}\zeta)^2\right)\hat{\mathbf{n}} + \partial_{ss}\zeta\,\hat{\mathbf{b}} \\
\hat{\mathbf{b}}' &= \hat{\mathbf{t}}' \times \hat{\mathbf{n}}' \approx -\partial_s\zeta\,\hat{\mathbf{t}} - \partial_{ss}\zeta\,\hat{\mathbf{n}} + \left(1 - \frac{1}{2}((\partial_s\zeta)^2 + (\partial_{ss}\zeta)^2)\right)\hat{\mathbf{b}}.
\end{aligned} \tag{8}$$

However, in general, the cross-section orientation can rotate independently of the transverse frame $\{\hat{\mathbf{n}}', \hat{\mathbf{b}}'\}$ [15]; we may express the rotated transverse frame as

$$\begin{pmatrix} \hat{\mathbf{d_1}} \\ \hat{\mathbf{d_2}} \end{pmatrix} = \begin{pmatrix} \cos\chi & \sin\chi \\ -\sin\chi & \cos\chi \end{pmatrix} \begin{pmatrix} \hat{\mathbf{n}} \\ \hat{\mathbf{b}} \end{pmatrix}. \tag{9}$$

The curvature is given by $\boldsymbol{\kappa} = \hat{\mathbf{t}} \times \partial_s \hat{\mathbf{t}}$ and the torsion by $\tau = \hat{\mathbf{d_2}} \cdot \partial_s \hat{\mathbf{d_1}}$; to find the new curvature $\boldsymbol{\kappa'}$ and torsion τ', derivatives are taken with respect to the new arclength parameter s', where $|\mathrm{d}\boldsymbol{\gamma'}/\mathrm{d}s'| = 1$. The rod free-energy H is given, to second order in ζ and χ, by

$$H \approx \frac{B}{2R^2}\int_0^{2\pi R} \mathrm{d}s \left[\chi^2 + \frac{C}{B}\left(\partial_{sss}\zeta + \partial_s\zeta + \partial_s\chi\right)^2 - \frac{M}{B\kappa}\left((\partial_{ss}\zeta)^2 - 2(\partial_s\zeta)^2 - \chi^2\right)\right]. \tag{10}$$

Note that choice of angle χ represents a gauge degree of freedom; it is convenient to choose $\chi = -\partial_{ss}\zeta - \partial_s\zeta + \tilde{\chi}$ so that

$$H \approx \frac{B}{2R^2}\int_0^{2\pi R} \mathrm{d}s \left[\left(1 + \frac{M}{B\kappa}\right)\left(\partial_{ss}\zeta + \partial_s\zeta - \tilde{\chi}\right)^2 + \frac{C}{B}\left(\partial_s\tilde{\chi}\right)^2 - \frac{M}{B\kappa}\left((\partial_{ss}\zeta)^2 - 2(\partial_s\zeta)^2\right)\right]. \tag{11}$$

Taking advantage of periodic boundary conditions, we expand ζ and $\tilde{\chi}$ in Fourier modes as

$$\begin{aligned}
\zeta &= \sum_{n=-\infty}^{\infty} \hat{\zeta}_n e^{ins/R}, \quad \hat{\zeta}_{-n} = \hat{\zeta}_n^* \\
\tilde{\chi} &= \sum_{n=-\infty}^{\infty} \hat{\tilde{\chi}}_n e^{ins/R}, \quad \hat{\tilde{\chi}}_{-n} = \hat{\tilde{\chi}}_n^*
\end{aligned} \tag{12}$$

which allows us to write the energy as a quadratic form:

$$H = \sum_{n=-\infty}^{\infty} (\hat{\zeta}_n\ \hat{\tilde{\chi}}_n)^\dagger \mathcal{H}_n (\hat{\zeta}_n\ \hat{\tilde{\chi}}_n) \tag{13}$$

where

$$\mathcal{H}_n = \begin{pmatrix} (n^2-1)^2 + \frac{M}{B\kappa} & \left(1 + \frac{M}{B\kappa}\right)(n^2-1) \\ \left(1 + \frac{M}{B\kappa}\right)(n^2-1) & 1 + \frac{M}{B\kappa} + \frac{C}{B}n^2 \end{pmatrix}. \tag{14}$$

Stability of the planar ring only holds when $\mathcal{H}_n$ is a positive-definite matrix. Thus, the stability threshold is given by

$$\det \mathcal{H}_n = n^2 \left[\frac{C}{B} \left(\frac{M}{B\kappa} + (n^2-1)^2 \right) - \frac{M}{B\kappa} \left(\frac{M}{B\kappa} + 1 \right) (n^2-2) \right] = 0 \, , \tag{15}$$

which results in the curves shown Fig.4(b) in the manuscript.

We now comment on the validity of the rod model in comparison to the experiments, which show a buckling instability at an aspect ratio of $\xi \approx 3$. While this aspect ratio is rather small for the slender rod approximation used in this model, we expect that the model is qualitatively correct. An indicator of the breakdown of the slender rod approximation comes from a comparison of the extensional energy $E_{\text{ext}} \sim VE(\Delta L/L)^2$, where $\Delta L/L$ is the strain due to changing the length L of the ring by ΔL, with the bending energy $E_{\text{bend}} \sim LB(\Delta\kappa)^2$ [16]. For small strains ϵ, $\Delta L \sim \epsilon L$ and $\Delta\kappa \sim \epsilon/R$. Since length $L \sim R$ and the volume $V \sim Ra^2$, the ratio of the two energies is given by

$$\frac{E_{\text{bend}}}{E_{\text{ext}}} \sim \frac{B}{ER^2a^2} \, . \tag{16}$$

In terms of the Young's modulus E, the bending modulus B scales with the second moment of area, $B \sim Ea^4$, so

$$\frac{E_{\text{bend}}}{E_{\text{ext}}} \sim \frac{a^2}{R^2} = \xi^{-2} \, . \tag{17}$$

Therefore, at $\xi = 3$, the bending energy is expected to be almost an order of magnitude smaller than the extensional energy.

References

[1] Ya-Wen Chang, Alexandros A Fragkopoulos, Samantha M Marquez, Harold D Kim, Thomas E Angelini, and Alberto Fernández-Nieves. Biofilm formation in geometries with different surface curvature and oxygen availability. *New J. Phys.*, 17(3):033017, 2015.

[2] E Pairam, H Le, and A Fernández-Nieves. Stability of toroidal droplets inside yield stress materials. *Phys. Rev. E.*, 90(2):021002, 2014.

[3] R. D. Groot and P. B. Warren. Dissipative particle dynamics: Bridging the gap between atomistic and mesoscopic simulation. *Journal of Chemical Physics*, 107(11):4423–4435, 1997.

[4] P. J. Hoogerbrugge and J. M. V. A. Koelman. Simulating microscopic hydrodynamic phenomena with dissipative particle dynamics. *Europhysics Letters*, 19(3):155–160, 1992.

[5] P. Español and P. Warren. Statistical-mechanics of dissipative particle dynamics. *Europhysics Letters*, 30(4):191–196, 1995.

[6] S. Nikolov, A. Fernández-Nieves, and A. Alexeev. Mesoscale modeling of microgel mechanics and kinetics through the swelling transition. *Applied Mathematics and Mechanics*, 39(1):47–62, 2018.

[7] Toyoichi Tanaka and David J. Fillmore. Kinetics of swelling of gels. *J. Chem. Phys.*, 70(3):1214–1218, 1979.

[8] Paul J. Flory and John Rehner Jr. Statistical mechanics of cross-linked polymer networks i. rubberlike elasticity. *J. Chem. Phys.*, 11(11):512–520, 1943.

[9] Paul J. Flory and John Rehner Jr. Statistical mechanics of cross-linked polymer networks ii. swelling. *J. Chem. Phys.*, 11(11):521–526, 1943.

[10] Masao Doi. Gel dynamics. *Journal of the Physical Society of Japan*, 78(5):052001, 2009.

[11] B. Erman and P. J. Flory. Critical phenomena and transitions in swollen polymer networks and in linear macromolecules. *Macromolecules*, 19(9):2342–2353, 1986.

[12] S. Hirotsu. *Coexistence of phases and the nature of first-order phase transition in poly-N-isopropylacrylamide gels*, pages 1–26. Springer, Berlin, Heidelberg, 1993.

[13] H. B. Callen. *Thermodynamics and an Introduction to Thermostatistics*. Wiley, 1985.

[14] M. S. Dimitriyev. *Function through form in soft matter: the influence of bounded geometries in heated gels and fluctuating proteins*. PhD thesis, Georgia Institute of Technology, School of Physics, 2017.

[15] B. Audoly and Y. Pomeau. *Elasticity and Geometry: From hair curls to the non-linear response of shells*. OUP Oxford, 2010.

[16] L.D. Landau, E.M. Lifshitz, A.M. Kosevich, and L.P. Pitaevskiĭ. *Theory of Elasticity*. Butterworth-Heinemann, New York, 1986.